3D insights into the structure and behaviour of Icelandic crystal mushes from gabbroic nodules

Rahul Subbaraman[1,*], Margaret E. Hartley[1], Jonathan Fellowes[1], Margherita Polacci[1], Barbara Bonechi[1], Lucia Pappalardo[2], Gianmarco Buono[2], David A. Neave[1]

[1]Department of Earth and Environmental Sciences, University of Manchester, Oxford Road, Manchester, M13 9PL, UK

[2]Istituto Nazionale di Geofisica e Vulcanologia – Osservatorio Vesuviano, Via Diocleziano, 328, 80125 Napoli, Italy

Author Emails:

rahul.subbaraman@manchester.ac.uk, margaret.hartley@manchester.ac.uk, jonathan.fellowes@manchester.ac.uk, margherita.polacci@manchester.ac.uk, barbara.bonechi@manchester.ac.uk, lucia.pappalardo@ingv.it, gianmarco.buono@ingv.it, david.neave@manchester.ac.uk

This is a non-peer-reviewed preprint submitted to *EarthArXiv*.
It has also been submitted for peer review to *Earth and Planetary Science Letters* and is currently under review. Subsequent versions may differ. If accepted, the final version will be available from the publisher with a DOI.

3D insights into the structure and behaviour of Icelandic crystal mushes from gabbroic nodules

Rahul Subbaraman[a,*], Margaret E. Hartley[a], Jonathan Fellowes[a], Margherita Polacci[a], Barbara Bonechi[a], Lucia Pappalardo[b], Gianmarco Buono[b], David A. Neave[a]

[a]*Department of Earth and Environmental Sciences, University of Manchester, Oxford Road, Manchester, M13 9PL, UK*
[b]*Istituto Nazionale di Geofisica e Vulcanologia - Osservatorio Vesuviano - Sezione di Napoli, Via Diocleziano, 328, 80125, Napoli NA, Italy*

Abstract

Crystal mushes are porous yet cohesive frameworks of crystals interspersed with interstitial melts that form the plumbing systems beneath many active volcanoes. Gabbroic nodules from Gígöldur, central Iceland, provide a unique window into the structure and degassing behaviour of mushy magma reservoirs - localised crystal mush domains beneath Icelandic volcanoes. These plagioclase-rich nodules formed through crystallisation, accumulation, and ascent within a stratified mush system, with their mafic components crystallising within interstitial spaces between a framework constructed from predominantly large plagioclase grains. The high vesicularity (21–30 vol.%) and extensive vesicle connectivity (>93%) of these nodules identified from XCT observations confirm that a free vapour phase was present at the surface. Saturation pressure estimates (2.75–3.75 kbar) indicate the melts in the nodules were volatile-saturated under their conditions of final storage ($\sim$ 2.3 $\pm$ 0.5 kbar, $\sim$ 7.8 $\pm$ 1.6 km). Despite significant degassing,

*Corresponding author
Email address: rahul.subbaraman@manchester.ac.uk (Rahul Subbaraman)

the rigid crystal framework and interconnected vesicle networks within the nodules preserve their structural integrity during ascent, as volatiles escape through these vesicle channels. However, where such channels are absent or disrupted, nodules may disaggregate into individual crystals in the final stages of ascent, potentially supplying the crystal cargo of plagioclase-ultraphyric basalts that erupt at Gígöldur. The nodules sample the buoyant, plagioclase-rich roof cumulates of a stratified mushy magma reservoir. These findings highlight the role of volatiles in mush dynamics, the evolution of stratified magma reservoirs, and the transport of crystalline material in Icelandic volcanic systems.
Keywords: Gabbroic Nodules, Crystal Mush, Magma Plumbing System, Plagioclase-rich Cumulates, Stratified Magma Reservoirs, Icelandic Volcanism

1. Introduction

Crystal mushes, cohesive yet porous frameworks of crystals interspersed with interstitial melts, are thought to form the plumbing systems beneath many active volcanoes (e.g., Annen et al., 2005; Edmonds et al., 2019). Transcrustal mush systems in continental settings are thought to be geometrically complex and vertically extensive (e.g., Cashman et al., 2017; Paulatto et al., 2019), whereas smaller, localised mushy magma reservoirs, in oceanic settings such as Iceland, may be vertically stacked and separated by melt-free country rock (e.g., Chamberlain et al., 2019; Maclennan, 2019). Ascending melts and exsolved fluids create small, potentially eruptible sills or melt lenses within these variably porous mushy domains (e.g., Holness et al., 2007). Understanding the pre- and syn-eruptive textures of crystal mushes is thus critical for refining models of magma behaviour (e.g., Bergantz et al., 2015; Sparks and Cashman, 2017), as their properties ultimately

determine whether magma erupts or remains within the crust. However, this undertaking is extremely challenging. Mush-derived clots of crystals often disaggregate during magma ascent (e.g., Hansen and Grönvold, 2000; Holness et al., 2007), while mushes preserved in fossil magma reservoirs are subject to overprinting by post-emplacement physical and chemical processes (e.g., Holness et al., 2017; O'Driscoll et al., 2010). In this context, gabbroic nodules, also known as cognate xenoliths, plutonic nodules, or crystalline enclaves (Holness et al., 2019), provide a unique opportunity to investigate the petrology of mushy magma reservoirs beneath basaltic volcanoes. While numerous studies have explored the 2D structure of mush fragments and mush-derived crystal clusters in basalts (e.g., Neave et al., 2014; Holness et al., 2019), analogous 3D studies remain to be undertaken. Such studies are essential for uncovering the spatial relationships and textural complexities of crystal mushes, offering deeper insights into magma reservoir dynamics.

Understanding the systematics of H_2O and CO_2 in crystal mushes is essential to deciphering their degassing behaviour within magma plumbing systems and their influence on magma ascent and crystal mush disaggregation. Volatiles, whether dissolved in magma or exsolved as bubbles, critically influence magma dynamics and eruptive activity (e.g., Edmonds and Wallace, 2017). As volatiles exsolve they form bubbles that, when preserved, become vesicles and provide vital clues about degassing processes. Studying vesicle textures is therefore a key approach to understanding volatile behaviour in magma systems. Vesicle size distributions (VSDs) are widely used to infer nucleation, growth and coalescence events during vesiculation (e.g., Klug and Cashman, 1994). Advances in X-ray computed microtomography (XCT), pioneered by Proussevitch et al. (1998), have

revolutionised vesicle studies, offering insights into outgassing dynamics, bubble coalescence, and magma ascent behaviour during eruptions. A deeper understanding of these processes is crucial for predicting eruptive behaviour and mitigating volcanic hazards. XCT analysis on volcanic samples from Stromboli, Villarrica, the Campanian Ignimbrite, Hunga Tonga-Hunga Ha'apai, Ambrym, and Las Sierras-Masaya demonstrated the value of XCT in tracking vesicle connectivity and vesicle number density (Bamber et al., 2024; Colombier et al., 2018; Polacci et al., 2008, 2009, 2012), crucial to understanding magma transport and degassing.

The entrainment of crystal mush fragments, driven by the fracturing of and dislodgement from their sources, remains poorly understood (Holness et al., 2019). Therefore, it is prudent to consider that erupted nodule populations may preferentially sample more fracture-prone mush domains. Additionally, these entrained mush fragments must maintain structural integrity to avoid disaggregating into macrocrysts in basalts (e.g., Hansen and Grönvold, 2000; Lange et al., 2013; Neave et al., 2014). Reconstructing mush textures and dynamics at depth requires careful analysis of erupted nodules for sampling biases. Most erupted nodules contain >60 vol.% crystals and <30 vol.% vesicles (Holness et al., 2019), controlled by the minimum crystal volume fraction needed to create a stable framework of randomly oriented grains and the structural weakening of high-porosity nodules as vesicularity increases (Coombs et al., 2003). Exsolved volatiles reduce the bulk density of magmas and facilitate their ascent, particularly in volatile-rich systems, but the expansion of this vapour phase without interstitial gas or melt removal may cause structural failure leading to nodule disaggregation, as observed in mafic enclaves within volcanic rocks (e.g., Bacon, 1986; Candela, 1991). These insights high-

light the need for detailed studies on gabbroic nodules to better understand how the crystal mush disaggregates and how this disaggregation affects volcanic processes.

Here, we focus on gabbroic nodules from Gígöldur in central Iceland, first reported by Hansen and Grönvold (2000). We use these nodules to address two key questions: (1) What do gabbroic nodules reveal about crystal mush texture and chemistry at depth? (2) How well do the gabbroic nodules retain structural integrity during ascent?

2. Samples and analytical methods

Gígöldur is a broad NNE-SSW-trending ridge of interlayered hyaloclastites and craters situated in the highlands north of Vatnajökull glacier, located between Bárðarbunga to the southwest and Askja to the northeast (Figure B1a; Hansen and Grönvold, 2000). Nodule samples were collected from two locations along the ridge, approximately 5 km apart, referred to as Gígöldur Central and Gígöldur South (Figure B1b). The nodules are 5-10 cm in diameter, are rounded to sub-angular, and are composed mainly of plagioclase aggregates encased in glass. They also contain small but variable amounts of interstitial olivine and occasionally dark green clinopyroxene. They exhibit high vesicularity and significant textural and compositional variability (Figure B1c). While most nodules were picked up loose from the float, some nodules were found *in situ* within plagioclase-phyric scoriaceous agglutinates (Figure B1d).

A summary of samples analysed in this study, including sample type and the analytical techniques applied, is provided in Supplementary Table B1. Two nod-

ules (GO19-01a.X and GO19-02.X), each about 10 cm in their longest dimension, were selected for further investigation, and four cylindrical rock cores were drilled from each nodule (Figure B2a). The optimal core diameter was determined by balancing structural integrity and resolution, ensuring that key features were preserved. Given the high vesicle content, multiple core diameters were systematically tested to assess their suitability. Smaller diameters (6.35 mm, 9.53 mm, and 12.7 mm) compromised structural stability of the cores, while diameters exceeding 20 mm would have increased scan times beyond the available funded access hours. Ultimately, a 15 mm diameter was selected as the most appropriate compromise. Core heights ranged from 16.7 mm to 27.5 mm to accommodate variations in nodule morphology while maintaining sample integrity. Cores with suffix C11, C12, C13, and C14 from nodule GO19-01a.X are designated as Batch-I, while the rest are referred to as Batch-II (Figure B2b).

A total of seven thin sections were prepared from areas between the cores of both nodules. Initial examination under transmitted light microscopy revealed olivine, clinopyroxene, and plagioclase grains. Plane-polarised light (PPL) images were captured at a high resolution of 5000 pixels per inch using a GX Microscopes PrimeScan system. Partial cross-polarised light (PXPL) and cross-polarised light (XPL) images were acquired with a uScope GX-1020 Geological Slide Scanner at polariser-analyser angles of 45° and 90°, respectively, using a ×10 magnification to enhance mineral contrast. The 45° angle provided a view where no silicate phase was in complete extinction, aiding mineral identification. The phase proportions of the rock were quantified through a modified point-counting method using the image analysis software JMicroVision v. 1.3.4 (Roduit, 2008). PPL or PXPL im-

ages of the thin sections were systematically segmented into equal-area rectangles. Successive grids were generated by subdividing the initial grid at its midpoints, enabling a detailed assessment of mineral distribution and precise quantification of all constituent phases across the thin sections. Back-scattered electron images were acquired using a FEI/Thermofisher Quanta 650 (E)SEM FEG instrument housed in the Williamson Research Centre, University of Manchester.

X-ray computed microtomography (XCT) was performed using a Carl Zeiss Xradia Versa-410 3D X-ray microscope at the Istituto Nazionale di Geofisica e Vulcanologia - Sezione di Napoli Osservatorio Vesuviano (INGV-OV), Naples, Italy. Scans were performed in absorption mode with 1601 projections collected over a 360° rotation at 90 kV and 8 W, and an optical magnification of $\times$0.4, resulting in a nominal voxel size of 16.0918μm. Data were reconstructed using XRMReconstructor, and vesicle and crystal geometries were characterised and quantified using Thermo Scientific™ Avizo v. 2019.1, and Fiji v1.54f. Details of the XCT analysis methods are provided in Appendix A. Our XCT analysis aimed to effectively distinguish the constituent phases—plagioclase, olivine, clinopyroxene, matrix glass, and vesicles—using a lab-based XCT setup. However, since we used absorption contrast mode and prioritised glass-plagioclase separation, olivine and clinopyroxene could not be distinguished in Batch-I, necessitating their combined classification as mafics in subsequent analyses and discussions.

Minerals and glasses were geochemically characterised in one representative thin section from each of the nodules discussed above. These thin sections were selected to minimise the presence of ash while ensuring that all major phases were

included. Additional mineral analyses were conducted on five additional nodule thin sections and three scoria thin sections, representing different sampling locations and textures to capture mineralogical variability. Glass analyses were performed on four nodule and two scoria thin sections from this set. Major and minor element compositions of minerals and glass were determined using electron probe microanalysis (EPMA) with a Cameca SX100 instrument housed at the Williamson Research Centre, University of Manchester. Details of the EPMA analytical procedure and secondary standards measurements are provided in Appendix B.

Magmatic H_2O and CO_2 concentrations were estimated using published data from volcanic systems chemically allied with Gígöldur (Supplementary Table B4). The OPAM thermobarometer (Higgins and Stock, 2024), based on melt (matrix glasses or melt inclusions) chemistry, was used to estimate pressure and temperature of storage, assuming equilibrium between the melt and the mineral assemblage olivine, plagioclase, and augitic clinopyroxene. Modal phase abundances from point counting were combined with calculated mineral densities to calculate the bulk density of the nodules. The methods for liquid and mineral density calculations are detailed in Appendix A.

3. Results

3.1. Petrography and point counting

Both nodules contain plagioclase, olivine, glass, and vesicles. Nodule GO19-01a.X additionally contains clinopyroxene, and GO19-02.X contains accessory Cr-spinels and occasional particulate volcanic ash (Figure B2c, d). Thin sections

from both the nodules exhibit significant textural variability. Plagioclase grains (100μm to >5 mm) primarily form clusters rather than isolated crystals and often host melt inclusions. BSE images reveal multiple generations of rims enclosing both individual plagioclase crystals and clusters (Figure B2e-g). Olivine grains are typically smaller (<1.5 mm) and are found interstitially between plagioclase clusters, often in the vicinity of vesicles. Clinopyroxene in GO19-01a.X is subhedral to sub-rounded, enclosed by plagioclase, and contains fractures and melt inclusions. Vesicles in both samples can be grouped into three distinct types: (1) small (<0.2 mm), circular, and non-coalesced; (2) moderate (0.2–1 mm) and partially coalesced; and (3) large (>1mm), irregular, and fully or partially coalesced. They are rimmed by glass with variable thickness. In GO19-02.X, some vesicles are partially filled with particulate volcanic ash. Cr-spinels are associated with plagioclase and olivine. A full set of thin section scans are available in Subbaraman et al. (2025a). Point-counting (average 3400 points) shows modal mineralogical classifications ranging from nearly anorthositic to leuco-troctolitic and leuco-gabbroic (Figure B3a–c).

3.2. X-ray computed microtomography (XCT) analysis

In Batch-I, vesicles were easily segmented from surrounding glass and crystals using simple thresholding, complemented by image segmentation techniques implemented in Avizo, like Erosion, Dilation, and Removal of Small Spots. Batch-II posed additional challenges due to vesicle infill by particulate volcanic ash, leading to an underestimation of vesicle abundance. Approximately 1 vol.% of pixels in Batch-I and 4 vol.% in Batch-II (mainly corresponding to volcanic ash fragments) remain unassigned. Individual plagioclase crystals show minimal phase contrast with neighbouring grains, meaning that individual plagioclase grains within

clusters could not be further segmented in either batch. Volumetric proportions from XCT data are presented in Figure B4a, with representative 3D renderings in Figure B4b, c. A full set of reconstructions is available in Subbaraman et al. (2025b).

3.2.1. Minerals and glasses

The mineralogical diversity across the samples, highlighted through 3D visualisation, is detailed in Supplementary Table B2. Batch-I cores mainly comprise plagioclase and mafics, while Batch-II cores include Cr-spinels. Phase proportions show no significant variability within each nodule. Batch-I has a ~65 vol.% crystal framework (plagioclase: 58 vol.%), whereas Batch-II contains ~58 vol.% crystal framework (plagioclase: 52.5 vol.%). Plagioclase grains within the framework are in contact with one another and have low aspect ratios (blocky or stubby), while mafic phases fill interstitial spaces between plagioclase clusters. Mafics in Batch-I appear larger, likely due to their clustering and the inability of the technique to resolve grain boundaries. Mafics in Batch-II are smaller and more uniformly distributed. Glass encloses plagioclase clusters and separates mafics, constituting 6.73 vol.% in Batch-I and 15.76 vol.% in Batch-II.

3.2.2. Vesicles

Following the application of geometrical filters, 3D volume analysis reveals vesicle sizes spanning approximately $10^4 \mu m^3$ (the lower limit of the technique resolution) to over $10^{10} \mu m^3$ (Supplementary Table B3); smaller vesicles may be present in the samples but could not be robustly identified. Vesicle textures show notable differences between the two batches, with lower variability within each batch. Batch-I has a mean vesicle content of ~27 vol.%, while Batch-II samples

contain ~22.5 vol.% vesicles. Vesicles were categorised by connectivity and size (Figure B4d; a full set of renderings in Subbaraman et al., 2025b). Connectivity, defined as the volume proportion of vesicles that are interconnected and extend to the core edge, is high across cores, ranging from 0.933 to 0.988 (Supplementary Table B3). Vesicles are divided into two broad categories based on size. Tiny vesicles (<10^6 μm^3), likely formed from syn-eruptive vesiculation during shallow ascent (Klug and Cashman, 1996), are irrelevant to the study of mushes and are not considered further. Large vesicles (>10^6 μm^3), likely originating from pre-eruptive bubble growth in magma chambers (Sparks and Brazier, 1982) or syn-eruptive coalescence (Klug and Cashman, 1994), are hence the focus of subsequent analysis. Large vesicles are further classified into three subgroups based on size and morphology, illustrated in the vesicle volume distribution (VVD) plots (Supplementary Figure B1). The first subgroup, Type I, includes vesicles with volumes from 10^8 to >10^{10} μm^3 and are characterised by irregular, tortuous shapes formed through partial or extensive coalescence around the crystal framework. Type II vesicles, ranging from a few ~10^6 to 10^8 μm^3, are sub-spherical to blob-like, displaying a botryoidal texture similar to a bunch of grapes. Finally, Type III vesicles, spanning a few 10^6 μm^3, feature nearly spherical to ellipsoidal shapes with partially coalesced forms. The vesicle size distribution (Figure B5a, b; Supplementary Figure B2) reveals that Type-II and Type-III vesicles across all samples exhibit a power-law distribution, with Batch-I samples having a significantly lower exponent (0.42) than Batch-II samples (0.70). Type-I vesicles with volumes ranging from 10^8 to 10^9 μm^3 show power-law distributions with contrasting exponents: 1.07 in Batch-I and 0.55 in Batch-II. For vesicles with volumes between 10^9 and 10^{10} μm^3, all samples exhibit either a power-law distribution with exponents much

greater than 1 (1.60 in Batch-I and 1.44 in Batch-II) or an exponential distribution.

3.3. Conditions of magma storage

All the chemical data used in this study are provided in Appendix B. Melt inclusions and matrix glasses in all our samples are basaltic in composition (Supplementary Figure B3). To obtain the context needed to evaluate the saturation state of volatiles and their degassing behaviour, as well as to understand nodule buoyancy, we estimated the P-T conditions under which mushes developed at depth. We used the empirical OPAM thermobarometer of Higgins and Stock (2024), which uses a statistical approach to assess the probability of melt OPAM saturation. We obtained a most likely pressure of ~.29 ± 0.47 kbar, corresponding to a depth of ~7.83 ± 1.57 km, and a temperature range of 1187–1229°C (Figure B6). Calculated densities of melts and minerals at the OPAM saturation pressures and temperatures are presented in Table B1.

3.4. Estimated magma volatile contents

To estimate magmatic H_2O concentrations, we compiled 209 data points from clinopyroxene-, olivine-, and plagioclase-hosted melt inclusions from Holuhraun and Skuggafjöll, which exhibit geochemical similarity and geographical proximity to Gígöldur (Bali et al. (2018); Neave et al. (2014); see Supplementary Table B4). As Ce data, commonly used as a proxy to reconstruct H_2O content in melts under undersaturated conditions (Michael, 1995), are unavailable for Gígöldur, we instead used relationships between H_2O and major oxides. Specifically, H_2O and MgO values show a well-defined positive correlation, allowing us to reconstruct H_2O using the equation: $H_2O = 0.0520 \times MgO$. This yields estimated H_2O concentrations of 0.3–0.5 wt% for the Gígöldur melts. For CO_2, which has

been argued to behave similarly to Ba during volatile-undersaturated magamtic evolution (e.g., Le Voyer et al., 2019), previous studies have shown that degassing homogenises melt inclusion C/Ba ratios despite variations in Ba concentrations (Matthews et al., 2021). A compilation of 368 melt inclusions from Borgarhraun, Heilagsdalsfjall, Holuhraun, and Skuggafjöll (Bali et al. (2018); Hauri et al. (2017); Matthews et al. (2021); Neave et al. (2014); see Supplementary Table B4) yielded maximum CO_2/Ba ratios of 79–115. Using the Ba content of nodule glass from Gígöldur (sample NAL443: 19 ppm; Hansen and Grönvold, 2000), we estimate a realistic maximum CO_2 content of 1500–2200 ppm in undersaturated Gígöldur melts (Supplementary Figure B3).

4. Discussions

4.1. Do nodules represent fragments of mushes?

3D observations of the nodules reveal that their crystal frameworks remained largely intact following eruption, indicating strong mechanical integrity (Figure B4b, c). The absence of apparent fabrics, such as foliation or lineation, in the nodules reinforces the overall stability of the crystal framework. Martin et al. (2006) studied mafic enclaves from the Kameni Islands (Greece) and observed that plagioclase crystals with high aspect ratios, such as acicular or tabular forms, often bend or crack due to brittle deformation caused by rapid vesicle expansion. In contrast, low-aspect-ratio crystals largely remained unaffected. They proposed that coarse-grained, low-aspect-ratio crystals form robust crystal frameworks capable of resisting rapid vesicle expansion, thereby preserving the framework as vesicular enclaves. The prevalence of low-aspect-ratio plagioclase in our nodules, as noted from petrographic observations (Figure B2c, d), similarly suggests that

the crystal framework is sufficiently robust to withstand stresses from vesiculation, maintaining its mechanical integrity. We also observe high connectivity (volume of pixels connected with the core edge) in both matrix glass (>90%) and vesicles (>93%), which implies the presence of efficient pathways for gas and melt escape.

The vesicle size distributions (Figure B5a, b; Supplementary Figure B2) observed across our samples offer key insights into the degassing behaviour of the Gígöldur system. Vesicles exceeding $10^9 \mu m^3$ display high power-law exponents (>1), reflecting a dominance of bubble coalescence, facilitating the formation of interconnected pathways for degassing. The exponential fits observed in some samples suggest that degassing approaches near-equilibrium conditions (Bai et al., 2008). We modelled closed-system degassing profiles for CO_2, H_2O, and CO_2+H_2O from depth to the surface (Figure B5c, d; Supplementary Figure B4) using the volatile degassing model of Iacono-Marziano et al. (2012), implemented in the VESIcal Python package (Iacovino et al., 2021). The simulations were run in 100 pressure decrements ranging from 16-30 bar. These profiles reveal that CO_2 and H_2O exsolve continuously but minimally during ascent through much of the crust from magma storage at depths corresponding to $\sim 2.3 \pm 0.5$ kbar, with most exsolution occurring at depths of a few hundred metres, immediately beneath the surface. As magma rises and pressure decreases, volatiles exsolve, forming bubbles. As these bubbles grow, they push against the surrounding crystal framework, potentially causing crystals to separate. When volatile content is high, the increased bubble number density accelerates coalescence within porous nodules, contributing further to the disaggregation of the crystal structure. Our 3D vesicle analysis, combined with simple degassing calculations, thus suggests that disaggregation from

nodules into individual crystals, where it occurs, is driven by bubble coalescence. This process may largely occur within the last few hundred metres of ascent and results in the discrete crystals observed in the scoriaceous agglutinates.

Our findings align with existing models of shallow magma degassing. The literature proposes three primary mechanisms for gas escape from shallow reservoirs: (1) bubble (and crystal) suspension at very high melt fractions, (2) volatile channel formation at moderate melt and large crystal fractions, and (3) capillary fracturing at very low melt fractions when melt pools are isolated (Degruyter et al., 2019). Based on 2D point counting of thin sections and 3D XCT analysis of cores, nearly all samples fall within the 'channel zone.' In this zone, bubble coalescence creates volatile channels, enabling gas escape without necessitating repacking or deformation (elastic, plastic, or brittle) of the crystalline framework. This is particularly relevant under near-surface conduit conditions.

With their rigid frameworks and efficient volatile escape pathways, we propose that the gabbroic nodules from Gígöldur preserve the mesoscale structure of deep mushes. The observed mechanical integrity and vesicle connectivity have likely prevented complete disaggregation into individual crystals, despite significant degassing.

4.2. What can we infer about mush structure and formation beneath Gígöldur?

Assuming CO_2 concentrations of 1500–2200 ppm, calculations using the volatile saturation model of Iacono-Marziano et al. (2012), implemented in the VESIcal Python package (Iacovino et al., 2021), indicate that melts from Gígöldur became saturated with a CO_2-rich vapour at 2.75–3.75 kbar (Table B2). These

pressures lie at or above the magma storage pressures estimated by OPAM barometry (~ 2.29 ± 0.47 kbar; Table B2). It is therefore likely that the mushes beneath Gígöldur contained low but non-zero volumes of exsolved CO_2-rich vapour at depth.

The complex nature of mushy magma reservoirs beneath Gígöldur is reflected in the multiple generations of rims that enclose individual plagioclase crystals and clusters. Rims around crystal clusters indicate that some clusters were mobilised from deeper mushy reservoirs and transported to shallower reservoirs, where they remained suspended alongside locally grown crystals. In this environment, transported clusters and *in situ* crystals may have developed overgrowth rims under similar conditions. The oscillatory zoning observed in some grains indicates crystallisation under evolving magmatic conditions. These zoning patterns suggest that the mush environment was dynamic. We suggest that the magma plumbing system beneath Gígöldur likely consisted of stacked mushy magma reservoirs, as illustrated in Figure B7a. Within each mushy magma reservoir, density-driven crystal segregation led to local stratification, with mafic cumulates (olivine and clinopyroxene) accumulating at the base and plagioclase grains and clusters-occasionally with mafic grains from deeper levels-floating towards the roof. This process is illustrated in MMR2 in Figure B7c. In deeper reservoirs (such as MMR1 in Figure B7d), that have already become stratified, the accumulation of plagioclase grains and clusters from depth enriches plagioclase-rich roof zones. Flowing magma then entrains buoyant plagioclase layers in deeper reservoirs (i.e. MMR1) and transports these crystals to shallower magma reservoirs (i.e. MMR2), delivering multiple populations of plagioclase (and mafics) to parts of the system

that will ultimately form the framework of erupted nodules. This process impacts the overall mineralogy of the stacked mushy magma reservoirs system, with the deeper layers becoming increasingly mafic and, the shallower layers becoming increasingly plagioclase-rich (Figure B7a).

Our model also aligns with independent studies of Icelandic crustal structure, which combine seismic observations and petrological modelling (Jenkins et al., 2018). These studies reveal a relatively uniform 20 km-thick crust, underlain by a lens-like layer of mantle-derived material, including olivine-rich ultramafic and gabbroic cumulates (Supplementary Figure B5). This stratigraphy is particularly pronounced near the Vatnajökull ice cap, where Gígöldur is located.

4.3. How are the nodules formed?

We propose that the formation of nodules beneath Gígöldur involves a sequence of crystallisation, accumulation, and ascent through the magma plumbing system, as depicted in Figure B7. The multiple generations of rims enclosing both individual plagioclase crystals and clusters suggest a complex history of nodule framework assembly across multiple magmatic environments. The scarcity of isolated plagioclase crystals within the crystal framework of the nodules (Figure B2c,d) suggests that nucleation was limited, with grains instead adhering together early, likely in deeper reservoirs or during ascent (Figure B7c, d). Textural evidence, including the rounded edges of plagioclase grains, suggests that they underwent partial resorption or mechanical abrasion, likely due to movement between reservoirs as they experienced varying temperatures, compositions, or crystallinity. The stratification of mushy magma reservoirs (MMRs) beneath Gígöldur (Figure B7a) likely played a key role in this process, where plagioclase preferentially accumu-

lated at the reservoir roofs while denser olivine- and clinopyroxene-rich cumulates settled at their bases. Nevertheless, statistical saturation models for olivine, plagioclase, and augite (OPAM) suggest that the melts retained equilibrium with these minerals at the final storage conditions in the shallow crust (Higgins and Stock, 2024). However, the irregular shapes and lack of layering among mafic phases, coupled with their confinement to interstitial spaces, indicate that mafic minerals within the Gígöldur gabbroic nodules predominantly crystallised after the plagioclase framework accumulated. Density calculations reveal that, even without volatile exsolution, the maximum density of the nodules remains lower than that of the carrier liquid, meaning that they are inherently buoyant. Consequently, these plagioclase-rich nodules require only mechanical dislodgement for mobilisation into erupting magma (Figure B7b). As nodules ascend, bubble nucleation, growth, and coalescence occur, which can lead to their disaggregation into individual crystals in the final ascent stages. However, many nodules remain intact, as their mechanical integrity and vesicle connectivity provide structural resilience, allowing them to persist as discrete crystal aggregates (Figure B7b).

5. Conclusions

This study examines the structural integrity of nodules during ascent and their insights into the chemistry and textures of crystal mushes. Gabbroic nodules beneath Gígöldur formed through a combination of crystallisation, mobilisation, entrainment, accumulation, and ascent within a stratified mushy magma plumbing system. They are plagioclase-rich, with later-crystallising mafic phases filling interstitial spaces.

Despite extensive degassing, their rigid crystal frameworks maintain structural integrity, while highly connected vesicles provide efficient degassing pathways. Buoyancy facilitates their transport, though bubble nucleation and coalescence may induce partial disaggregation. However, many nodules remain intact, preserving primary mush textures. Where vesicle connectivity is poor, complete disaggregation may generate plagioclase-phyric crystal cargoes akin to Plagioclase Ultraphyric Basalts (PUBs; Lange et al., 2013).

The magma plumbing system beneath Gígöldur comprises stacked mushy magma reservoirs with stratification formed through density-driven segregation. Plagioclase entrainment from deeper levels likely influences mineralogical variation, with ultramafic cumulates at depth transitioning to gabbroic compositions at mid-levels and plagioclase-rich layers near the surface. Saturation pressure estimates indicate that the melts hosting these nodules were volatile-saturated at their final storage conditions.

This study provides a rare perspective into the structure and behaviour of mushy magma reservoirs in an active volcanic setting, demonstrating how crystal framework strength, melt connectivity, and volatile pathways govern nodule transport and preservation. The Gígöldur nodules confirm that crystal mushes can retain mesoscale integrity during ascent, constraining the mechanical properties of mush frameworks and their response to volatile exsolution. These findings enhance our understanding of crystal mush formation, evolution, and fragmentation and clarify the role of volatile-melt-crystal interactions in stratified mushy magma reservoirs beneath Icelandic volcanoes.

Acknowledgement

This publication results from work carried out under Trans-National Access action under the support of EXCITE - EC - HORIZON 2020 - INFRAIA 2020 Integrating Activities for Starting Communities under grant agreement N.101005611. Part of the EPMA data acquisition was conducted during the NERC Advanced Training Short Course in Quantitative X-ray Microanalysis in Earth and Environmental Sciences, funded by NERC grant NE/Y00373X/1. DAN acknowledges support from NE/T011106/1. MH acknowledges support from NERC grant NE/P002331/1. MP and BB acknowledge support from UKRI grant 4DVOLC (MR/V023985/1). RS thanks Lee Paul and David Oliver for their support with sample preparation.

Appendix A. Methodological details

A.1. X-ray computed microtomography (XCT) Methodology

A.1.1. Data Acquisition or Imaging

X-ray computed tomography (XCT) was conducted using a Carl Zeiss Xradia Versa-410 3D X-ray microscope at the Istituto Nazionale di Geofisica e Vulcanologia—Sezione di Napoli Osservatorio Vesuviano (INGV-OV) in Naples, Italy. Scans were performed in absorption mode, capturing 1601 projections over a 360° rotation at 90 kV and 8 W. The optical magnification was 0.4×, yielding a nominal voxel size of 16.0918μm. The detailed experimental setup is summarised in Table A1.

Table A1: XCT scan parameters

Sample	Source (KW)	Power (W)	SD (mm)	DD (mm)	Lens	Pixel size (μm)	Exp. Time (s)	Proj.	Filter	BHC
G019-01a-C1	90	8	-48	155	0.4X	16.0918	2.5	1601	LE5	0.2
G019-01a-C2	90	8	-48	155	0.4X	16.0918	2.5	1601	LE5	0.2
G019-01a-C3	90	8	-48	155	0.4X	16.0918	2.5	1601	LE5	0.2
G019-01a-C4	90	8	-48	155	0.4X	16.0918	2.5	1601	LE5	0.2
G019-02-C1	90	8	-48	155	0.4X	16.0918	3.0	1601	LE6	0.2
G019-02-C2	90	8	-48	155	0.4X	16.0918	3.0	1601	LE6	0.2
G019-02-C3	90	8	-48	155	0.4X	16.0918	3.25	1601	LE6	0.2
G019-02-C4	90	8	-48	155	0.4X	16.0918	3.0	1601	LE6	0.2

SD = Source-Sample distance, DD = Detector-Sample distance, Exp. Time = Exposure Time, Proj. = Projections.

A.1.2. Data reconstruction and pre-processing

Attenuation data were reconstructed using the filtered back-projection algorithm in XRMReconstructor (Xradia proprietary software), producing 1014 cross-sectional grayscale images per sample. Image processing, as well as vesicle and crystal geometry characterisation, were conducted using Thermo Scientific™ Avizo v. 2019.1 and Fiji v1.54f (an open-source image processing package). The initial 16-bit grayscale CT slices were converted to 8-bit grayscale TIFF format in Fiji, ensuring consistency in grayscale values for segmentation. The largest attainable cylindrical Volume of Interest (VOI) was cropped using Avizo's Cylinder Handle Box tool, followed by additional cropping of the top and bottom regions using the Crop Editor tool to exclude areas affected by residual cone beam hardening artefacts.

A.1.3. Image Segmentation and Analysis

Image segmentation involves distinguishing different materials or phases within the 3D volume scan based on voxel intensities. Segmentation was manually adjusted using the Interactive Thresholding tool, followed by processing with image segmentation tools such as Erosion, Dilation, Arithmetic, and Remove Small Spots. The segmented images were then analysed to quantify volume fractions, distribution, connectivity, and geometrical characteristics of various phases.

A.1.4. Geometrical filters used for vesicle segmentation

Geometric filtering of vesicles in this study relies on analysing their anisotropy, elongation, and flatness—geometric properties that characterise shape and orientation. These parameters are derived from the covariance matrix of the vesicle's point distribution, where each pixel's coordinates (c_{i1}, c_{i2}, c_{i3}) contribute to the matrix computation using the formula $\Sigma = \frac{1}{N}\sum_{i=1}^{N}(c_i - \mu)(c_i - \mu)^T$, with μ representing the mean of the distribution. The covariance matrix yields eigenvectors v_i that indicate principal directions of maximal variance, alongside eigenvalues $\lambda_1 \geq \lambda_2 \geq \lambda_3 > 0$, which quantify variance along these directions. Anisotropy measures deviation from spherical symmetry and is calculated as $1 - \sqrt{\lambda_3/\lambda_1}$. Elongation quantifies stretching along the primary axis relative to overall spread, given by $\sqrt{\lambda_2/\lambda_1}$. Flatness assesses similarity to a flat plane in 3D space, calculated as $\sqrt{\lambda_3/\lambda_2}$. For a vesicle to be considered valid, all eigenvalues must be positive (λ_i >0), ensuring meaningful elongation and flatness values within 0 < Elongation or Flatness ≤ 1, and anisotropy values should fall within 0 ≤ Anisotropy < 1. Vesicles outside these ranges were excluded as they likely represent data anomalies or measurement errors.

A.2. Thermobarometry

A user-friendly R script by Higgins and Stock (2024) was employed to implement their OPAM thermobarometer calibration, specifically designed for melts equilibrated with the olivine-plagioclase-augitic clinopyroxene assemblage. The script processed melt inclusion and matrix glass compositional data from nodule and scoria samples, stored in a CSV file, enabling precise P-T estimates for the studied melt compositions using the following equations:

$$\begin{aligned} P(\text{kbar}) = {} & 90.17 - (258.61X_{SiO_2}) + (34.47X_{AlO_{1.5}}) + (107.40X_{MgO}) \\ & - (191.57X_{CaO}) - (50.28X_{NaO_{0.5}}) + (191.90(X_{SiO_2})^2) \end{aligned} \tag{A.1}$$

$$\begin{aligned} T(^\circ\text{C}) = {} & -6807.12 + (7805.36X_{SiO_2}) + (5364.02X_{FeO}) + (8395.40X_{MgO}) \\ & + (6146.55X_{NaO_{0.5}}) + (8280.95X_{KO_{0.5}}) + (7251.05Al\#) \\ & + (17637.90(X_{SiO_2}X_{TiO_2})) + (1019.36(X_{CaO}X_{AlO_{1.5}})) \end{aligned} \tag{A.2}$$

where X followed by the oxide subscript denotes liquid cation fractions calculated using the method outlined in Table 1 of Putirka (2008). All pressure (kbar) estimates were converted to depth (km) relative to the surface using a second-order polynomial equation:

$$\text{Depth (km)} = -0.02777 \cdot P(\text{kbar})^2 + 3.48662 \cdot P(\text{kbar}) \tag{A.3}$$

A.3. Density Calculations

A.3.1. Density of Liquids

The density of the liquids is calculated using the author's own Python code based on DensityX (Iacovino and Till, 2019), based on the formulation:

$$\rho(P,T) = \sum_{ox} \frac{X_{ox} \times MW_{ox}}{X_{ox} \times \left(\overline{V}_{ox} + \frac{d\overline{V}}{dT} \left(T_{\text{inp}} - T_{\text{ref}} \right) + \frac{d\overline{V}}{dP} \left(P_{\text{inp}} - 1 \right) \right)} \tag{A.4}$$

where X_{ox} is the mole fraction of the oxides, MW_{ox} is the molecular weight of the oxides, $\overline{V}_{ox}$ is the molar volume of the oxide at reference conditions, $d\overline{V}/dP$ is the derivative of molar volume with respect to temperature, $d\overline{V}/dP$ is the derivative of molar volume with respect to pressure, T_{inp} is temperature (in K), T_{ref} is the reference temperature (in K), P_{inp} is pressure in bars. The parameters used in this calculation are given in Table A2.

Table A2: Parameters for oxide components to calculate density of liquids.

Oxide	Molar Mass (g/mol)	$\overline{V}_{ox}$ (cm^3/mol)	$d\overline{V}/dT$ (cm^3/mol-K)	$d\overline{V}/dP$ (cm^3/mol-bar)	Temperature (K)
SiO_2	60.0855	26.86	0.0	-1.89×10^{-4}	1773
TiO_2	79.88	28.32	7.24×10^{-3}	-2.31×10^{-4}	1773
Al_2O_3	101.96	37.42	2.62×10^{-3}	-2.26×10^{-4}	1773
FeO	71.85	12.68	3.69×10^{-3}	-4.50×10^{-5}	1723
MgO	40.3	12.02	3.27×10^{-3}	2.70×10^{-5}	1773
CaO	56.08	16.90	3.74×10^{-3}	3.40×10^{-5}	1773
Na_2O	61.98	29.65	7.68×10^{-3}	-2.40×10^{-4}	1773
K_2O	94.2	47.28	1.21×10^{-2}	-6.75×10^{-4}	1773
H_2O	18.02	22.9	9.50×10^{-3}	-3.20×10^{-4}	1273

Partial molar volumes $\overline{V}_{ox}$ for: SiO_2, Al_2O_3, MgO, CaO, Na_2O, K_2O at T_{ref} = 1773 K (Lange, 1997); TiO_2, at T_{ref} = 1773 K (Lange and Carmichael, 1987); FeO at T_{ref} = 1723 K Guo et al. (2014); H_2O at T_{ref} = 1273 K (Ochs III and Lange, 1999). $d\overline{V}/dT$ values for: SiO_2, TiO_2, Al_2O_3 from (Lange and Carmichael, 1987); MgO, CaO, Na_2O, K_2O from (Lange, 1997); FeO from Guo et al. (2014); H_2O from Ochs III and Lange (1999). $d\overline{V}/dP$ values for anhydrous components from Kress and Carmichael (1991); H_2O from Ochs III and Lange (1999).

A.3.2. Density of Minerals

The pressure and temperature dependence of mineral volumes is represented with the following equation (Berman, 1988):

$$\frac{V(P,T)}{V_r} = 1 + v_1(P - P_r) + v_2(P - P_r)^2 + v_3(T - T_r) + v_4(T - T_r)^2 \quad \text{(A.5)}$$

where v_1–v_4 are empirical fit parameters, and V_r and ρ_r are the molar volume and density of the minerals at the reference pressure (1 bar) and temperature (298.15 K). Considering law of conservation of mass,

$$\frac{V(P,T)}{V_r} = \frac{\rho_r}{\rho(P,T)} \quad \text{(A.6)}$$

Hence, density as a function of pressure and temperature is calculated as:

$$\rho(P,T) = \rho_r / \left[1 + v_1(P - P_r) + v_2(P - P_r)^2 + v_3(T - T_r) + v_4(T - T_r)^2\right] \quad \text{(A.7)}$$

The values of the constants used in Equation A.7 are provided in Table A3. Chemical data from EPMA analysis are used to calculate the molar proportions of the end-member compositions of feldspar, olivine, and clinopyroxene. These compositions are then combined with the densities calculated using the formula in Equation A.7 to determine the densities of the individual mineral phases.

Appendix B. Supplementary materials

The following is the Supplementary material related to this article.

MMC 1. A file containing supplementary figures and supplementary tables referred to in the main article.

MMC 2. A file containing EPMA setup and chemical analyses of secondary standards.

Table A3: Physical properties of minerals to calculate the density. v_1, v_2, v_3, and v_4 are coefficients for calculating mineral volume at a given pressure and temperature (Berman, 1988), and ρ_r is the molar density of the mineral phases at 1 bar and 298.15 K (Smyth and McCormick, 1995).

PHASE	MINERAL	v_1	v_2	v_3	v_4	ρ_r (g/cm^3)
Feldspar	Albite (Ab)	-1.95×10^{-6}	0	2.50×10^{-5}	6.72×10^{-9}	2.621
	Anorthite (An)	-1.27×10^{-6}	3.18×10^{-12}	1.09×10^{-5}	4.20×10^{-9}	2.765
	Orthoclase (Or)	-1.81×10^{-6}	5.11×10^{-12}	1.51×10^{-5}	5.49×10^{-9}	2.571
Olivine	Forsterite (Fo)	-7.91×10^{-7}	1.35×10^{-12}	2.65×10^{-5}	8.86×10^{-9}	3.227
	Fayalite (Fa)	-7.30×10^{-7}	0	2.65×10^{-5}	7.95×10^{-9}	4.402
Clinopyroxene	Wollastonite (Wo)	-1.25×10^{-6}	3.11×10^{-12}	2.82×10^{-5}	0	2.937
	Enstatite (En)	-7.50×10^{-7}	4.48×10^{-13}	1.42×10^{-5}	3.64×10^{-8}	3.204
	Ferrosilite (Fs)	-9.90×10^{-7}	0	3.18×10^{-5}	7.59×10^{-9}	4.002

MMC 2. A file containing EPMA chemical analyses of matrix glasses, melt inclusions, and the median mineral data used for thermobarometry and density calculations referred to in the main article.

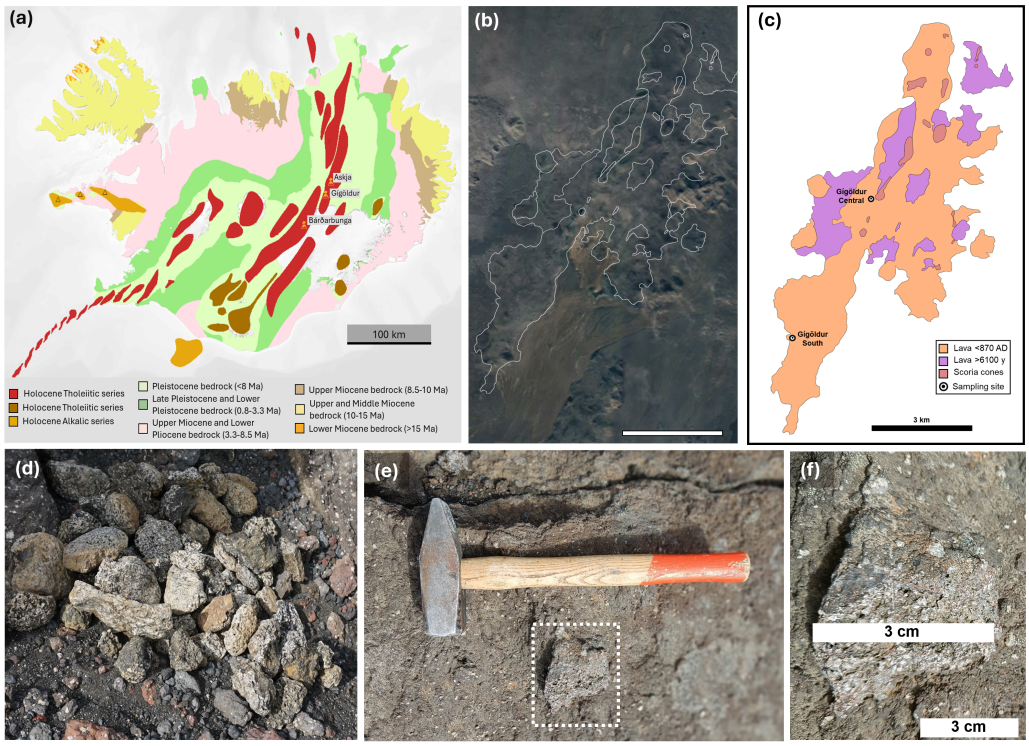

Figure B1: Geological context of gabbro nodules. (a) Geological map of Iceland showing the distribution of baserocks and Holocene lava flows, modified after Jakobsson et al. (2008) and Jóhannesson and Sæmundsson (2009). (b) Satellite image of Gígöldur and surrounding areas sourced from Google Earth Pro (2025), with the lithology boundaries obtained from Sigurgeirsson et al. (2015). (c) Field photograph illustrating the range of compositional and textural variability in the nodules. (d) Nodule observed *in situ*.

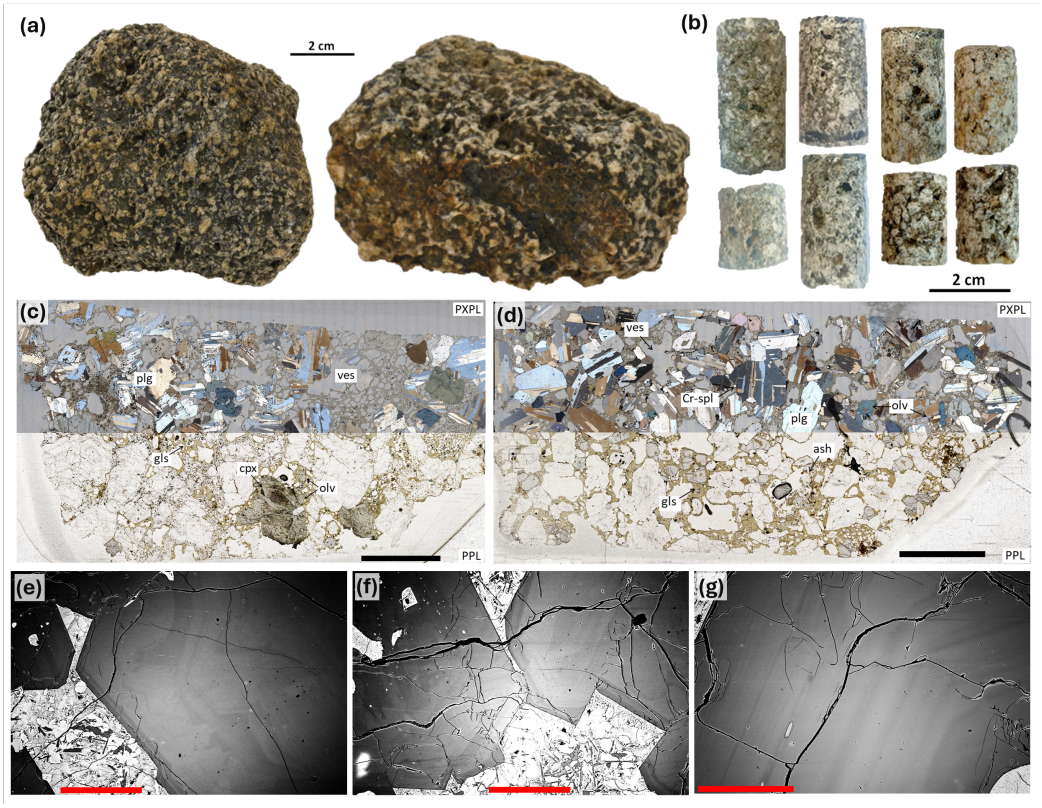

Figure B2: Samples analysed in this study. (a) Nodule samples GO19-01a.X (left) and GO19-02.X (right). (b) Rock cores extracted from the two nodules. (c) and (d) Representative thin sections of GO19-01a.X and GO19-02.X nodules, respectively, with the top half shown under partial cross-polarised light (PXPL; polariser-analyser at 45°) and the bottom half under plane-polarised light (PPL), with constituent phases marked. The black scale bar represents 5000μm. (e), (f), and (g) Backscattered electron (BSE) images of plagioclase grains in different samples, highlighting complex zonation patterns, including multiple generations of rims enclosing both individual crystals and crystal clusters. The red scale bar represents 200μm.

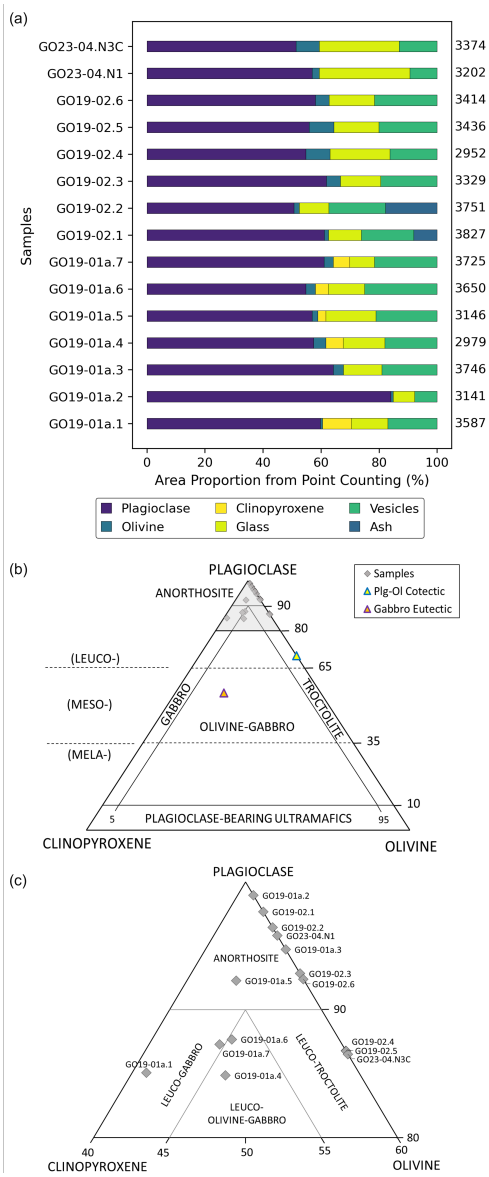

Figure B3: Constituents and classification of nodules. (a) Area phase proportion normalised to 100%, with the number of points sampled indicated for each sample. (b) IUGS gabbroic rock classification in a plagioclase-olivine-clinopyroxene ternary plot, showing compositional fields, gabbro eutectic, and olivine-plagioclase cotectic compositions. (c) Expanded view of the shaded region in (b) showing sample distribution.

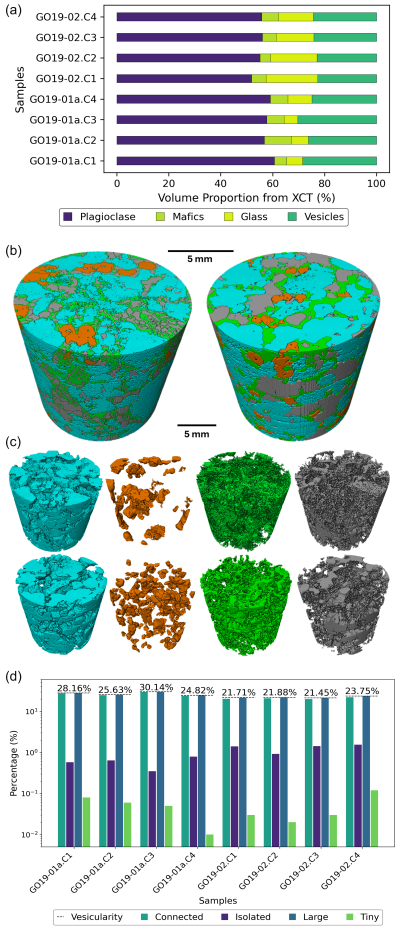

Figure B4: Results of XCT analysis. (a) Volume phase proportions normalised to 100%. (b) Representative 3D reconstructions with all phases combined. (c) Representative 3D reconstructions with individual phases separated. (d) Bar chart of vesicles categorised by connectivity and size. The vesicularity of the samples is indicated above the dashed line, which represents the vesicularity values.

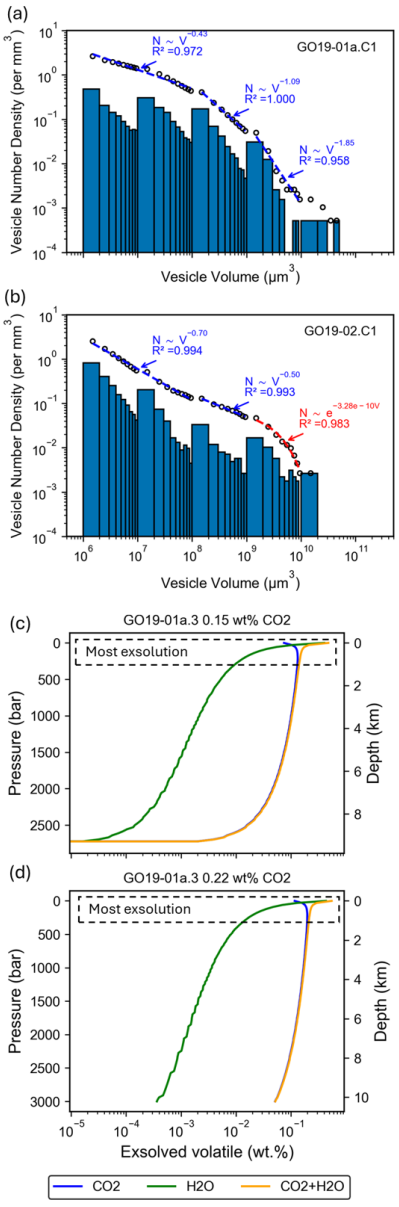

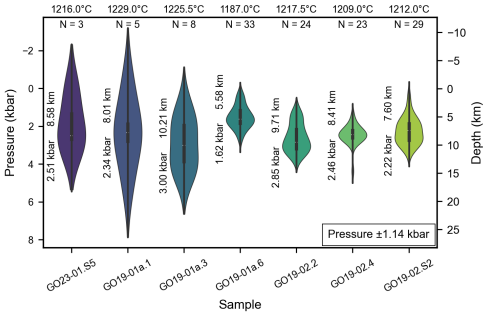

Figure B5: Connecting the vesicle growth dynamics and volatile degassing process. (a), (b) Cumulative (circles) and non-cumulative (bars) vesicle size distributions for two analysed cores, illustrating the full spectrum of vesicle growth characteristics observed in this study. (c),(d) closed-system degassing profiles using the volatile degassing model of Iacono-Marziano et al. (2012) for CO_2, H_2O, and CO_2+H_2O from final storage depth to surface conditions for (c) melt saturated and (b) melt unsaturated in CO_2-rich vapour.

Figure B6: Results from the Higgins and Stock (2024) OPAM thermobarometer, showing the distribution of pressure and corresponding depths of final storage for each sample. The number of data points and median temperature are annotated for each sample. The median pressure and depth for each sample are indicated next to the respective violin plots.

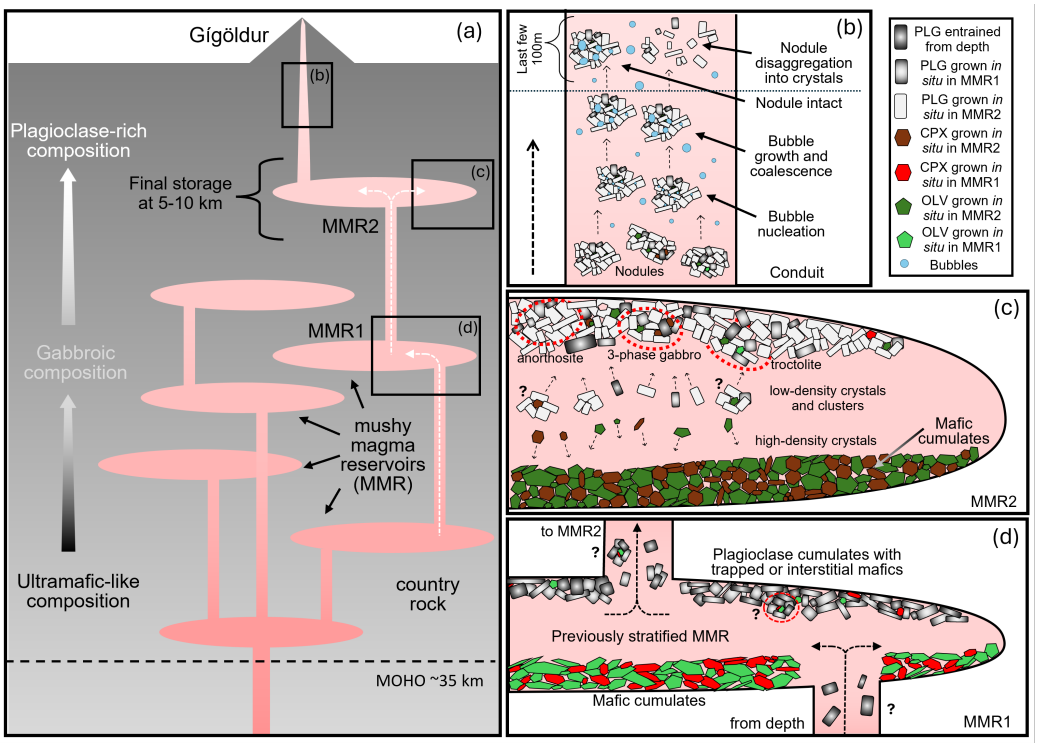

Figure B7: Mushes beneath Gígöldur and nodule formation. (a) Schematic representation of the magma plumbing system beneath Gígöldur, showing stacked mushy magma reservoirs (MMRs), with final storage occurring in an MMR at a depth of 5–10 km. (b) Ascent of nodules through the conduit, during which bubble nucleation, growth, and coalescence occur. In the final stages of ascent, the nodule may either remain intact or disaggregate into individual crystals. (c) Density-driven crystal segregation within the MMRs leads to the accumulation of plagioclase at the reservoir roof, incorporating both in situ-grown plagioclase and entrained crystals from depth. Olivine- and clinopyroxene-rich cumulates settle at the base of MMR2, the final storage reservoir, with olivine and clinopyroxene interstitially growing between the plagioclase clusters. (d) A detailed view of MMR1, a previously stratified magma reservoir, illustrating the influx of plagioclase from deeper levels. This includes the ascent of both *in situ*-grown plagioclase from MMR1 and entrained populations that ascend toward MMR2.

Table B1: Density calculations and proportions from point counting for nodule samples and carrier liquid at the final storage temperature. The maximum nodule density corresponds to the case where no vesicles are present.

Sample Name	Density Calculations (g/cm^3)					Proportions from Point Counting (%)						Nod (max)
	LIQ	MG	OLV	CPX	PLG	MG	OLV	CPX	PLG	ASH	VES	
GO19-01a.1	2.725	2.705	3.340	3.000	2.533	12.7	0.7	9.8	59.8	0.0	17.0	2.621
GO19-01a.3	2.736	2.739	3.253	-	2.551	13.2	3.6	0.0	64.2	0.0	19.0	2.613
GO19-01a.6	2.724	2.714	3.315	3.004	2.521	12.5	3.3	4.4	54.8	0.0	25.0	2.616
GO19-02.2	2.736	2.737	3.263	-	2.540	10.2	1.9	0.0	50.5	17.8	19.6	2.650
GO19-02.4	2.732	2.732	3.253	-	2.547	20.7	8.3	0.0	54.8	0.0	16.2	2.663
GO23-04.N3C	2.687	2.685	3.256	-	2.541	27.5	8.0	0.0	51.4	0.0	13.1	2.652

LIQ: liquid, MG: matrix glass, OLV: olivine, CPX: clinopyroxene, PLG: plagioclase, Nod: Nodule, CL: Carrier Liquid.

Table B2: Summary of volatile calculations in the mush. T_{OPAM}/P_{OPAM} refers to the temperature and pressure of OPAM saturation determined through thermobarometry. P_{SAT} represents the CO_2 saturation pressure. $CO_{2Isobar}$ or H_2O_{Isobar} denotes the isobaric compositions of CO_2 and H_2O at P_{OPAM}.

Sample	H_2O (wt%)	CO_2 (wt%)	P_{OPAM} (bar)	T_{OPAM} (K)	P_{SAT} (bar)	H_2O_{Isobar} (wt%)	$CO_{2Isobar}$ (wt%)	Saturation Test	$CO_{2excess}$ (ppm)
GO19-01a.1	0.408	0.150	2340	1229	2774	0.408	0.1220	Saturated	280
		0.220			3746.13		0.1224	Saturated	976
GO19-01a.3	0.407	0.150	3000	1225.5	2751	0.407	0.1669	Unsaturated	-
		0.220			3715.21		0.1675	Saturated	524
GO19-01a.6	0.387	0.150	1620	1187	2787	0.387	0.0788	Saturated	712
		0.220			3756.34		0.790	Saturated	1409
GO19-02.2	0.417	0.150	2850	1217.5	2752	0.417	0.1565	Unsaturated	-
		0.220			3715.78		0.1571	Saturated	629
GO19-02.4	0.411	0.150	2460	1209	2784	0.411	0.1289	Saturated	211
		0.220			3755.45		0.1293	Saturated	906

References

C. Annen, J. D. Blundy, R. S. J. Sparks, The genesis of intermediate and silicic magmas in deep crustal hot zones, Journal of Petrology 47 (2005) 505–539. doi:https://doi.org/10.1093/petrology/egi084.

M. Edmonds, K. V. Cashman, M. Holness, M. Jackson, Architecture and dynamics of magma reservoirs, Philosophical Transactions of the Royal Society A: Mathematical, Physical and Engineering Sciences 377 (2019) 20180298. URL: http://dx.doi.org/10.1098/rsta.2018.0298. doi:https://doi.org/10.1098/rsta.2018.0298.

K. V. Cashman, R. S. J. Sparks, J. D. Blundy, Vertically extensive and unstable magmatic systems: A unified view of igneous processes, Science 355 (2017). URL: http://dx.doi.org/10.1126/science.aag3055. doi:10.1126/science.aag3055.

M. Paulatto, M. Moorkamp, S. Hautmann, E. Hooft, J. V. Morgan, R. S. J. Sparks, Vertically extensive magma reservoir revealed from joint inversion and quantitative interpretation of seismic and gravity data, Journal of Geophysical Research: Solid Earth 124 (2019) 11170–11191. URL: http://dx.doi.org/10.1029/2019JB018476. doi:10.1029/2019jb018476.

K. J. Chamberlain, J. Barclay, K. J. Preece, R. J. Brown, J. P. Davidson, Lower crustal heterogeneity and fractional crystallization control evolution of small-volume magma batches at ocean island volcanoes (ascension island, south atlantic), Journal of Petrology 60 (2019) 1489–1522. URL: http://dx.doi.org/10.1093/petrology/egz037. doi:10.1093/petrology/egz037.

J. Maclennan, Mafic tiers and transient mushes: evidence from iceland, Philosophical Transactions of the Royal Society A: Mathematical, Physical and Engineering Sciences 377 (2019) 20180021. URL: http://dx.doi.org/10.1098/rsta.2018.0021. doi:10.1098/rsta.2018.0021.

M. B. Holness, A. T. Anderson, V. M. Martin, J. Maclennan, E. Passmore, K. Schwindinger, Textures in partially solidified crystalline nodules: a window into the pore structure of slowly cooled mafic intrusions, Journal of Petrology 48 (2007) 1243–1264. URL: http://dx.doi.org/10.1093/petrology/egm016. doi:10.1093/petrology/egm016.

G. W. Bergantz, J. M. Schleicher, A. Burgisser, Open-system dynamics and mixing in magma mushes, Nature Geoscience 8 (2015) 793–796. URL: http://dx.doi.org/10.1038/ngeo2534. doi:10.1038/ngeo2534.

R. S. J. Sparks, K. V. Cashman, Dynamic magma systems: Implications for forecasting volcanic activity, Elements 13 (2017) 35–40. URL: http://dx.doi.org/10.2113/gselements.13.1.35. doi:10.2113/gselements.13.1.35.

H. Hansen, K. Grönvold, Plagioclase ultraphyric basalts in iceland: the mush of the rift, Journal of Volcanology and Geothermal Research 98 (2000) 1–32. URL: http://dx.doi.org/10.1016/s0377-0273(99)00189-4. doi:10.1016/s0377-0273(99)00189-4.

M. B. Holness, Z. Vukmanovic, E. Mariani, Assessing the role of compaction in the formation of adcumulates: a microstructural perspective, Journal of Petrol-

ogy 58 (2017) 643–673. URL: http://dx.doi.org/10.1093/petrology/egx037. doi:10.1093/petrology/egx037.

B. O'Driscoll, C. H. Emeleus, C. H. Donaldson, J. S. Daly, Cr-spinel seam petrogenesis in the rum layered suite, nw scotland: Cumulate assimilation and in situ crystallization in a deforming crystal mush, Journal of Petrology 51 (2010) 1171–1201. URL: http://dx.doi.org/10.1093/petrology/egq013. doi:10.1093/petrology/egq013.

M. B. Holness, M. J. Stock, D. Geist, Magma chambers versus mush zones: constraining the architecture of sub-volcanic plumbing systems from microstructural analysis of crystalline enclaves, Philosophical Transactions of the Royal Society A: Mathematical, Physical and Engineering Sciences 377 (2019) 20180006. URL: http://dx.doi.org/10.1098/rsta.2018.0006. doi:10.1098/rsta.2018.0006.

D. A. Neave, J. Maclennan, M. E. Hartley, M. Edmonds, T. Thordarson, Crystal storage and transfer in basaltic systems: the skuggafjöll eruption, iceland, Journal of Petrology 55 (2014) 2311–2346. URL: http://dx.doi.org/10.1093/petrology/egu058. doi:10.1093/petrology/egu058.

M. Edmonds, P. J. Wallace, Volatiles and exsolved vapor in volcanic systems, Elements 13 (2017) 29–34. URL: http://dx.doi.org/10.2113/gselements.13.1.29. doi:10.2113/gselements.13.1.29.

C. Klug, K. V. Cashman, Vesiculation of may 18, 1980, mount st. helens magma, Geology 22 (1994) 468–472. URL: http://dx.doi.org/

10.1130/0091-7613(1994)022<0468:VOMMSH>2.3.CO;2. doi:10.1130/0091-7613(1994)022<0468:VOMMSH>2.3.CO;2.

A. Proussevitch, R. Ketcham, W. Carlson, D. Sahagian, Preliminary results of x-ray ct analysis of hawaiian vesicular basalts, Eos 79 (1998) 360.

E. C. Bamber, G. La Spina, F. Arzilli, M. Polacci, L. Mancini, M. de' Michieli Vitturi, D. Andronico, R. A. Corsaro, M. R. Burton, Outgassing behaviour during highly explosive basaltic eruptions, Communications Earth and Environment 5 (2024). URL: http://dx.doi.org/10.1038/s43247-023-01182-w. doi:10.1038/s43247-023-01182-w.

M. Colombier, B. Scheu, F. B. Wadsworth, S. Cronin, J. Vasseur, K. J. Dobson, K. Hess, M. Tost, T. I. Yilmaz, C. Cimarelli, M. Brenna, B. Ruthensteiner, D. B. Dingwell, Vesiculation and quenching during surtseyan eruptions at hunga tonga-hunga ha'apai volcano, tonga, Journal of Geophysical Research: Solid Earth 123 (2018) 3762–3779. URL: https://doi.org/10.1029/2017JB015357. doi:10.1029/2017jb015357.

M. Polacci, D. R. Baker, L. Bai, L. Mancini, Large vesicles record pathways of degassing at basaltic volcanoes, Bulletin of Volcanology 70 (2008) 1023–1029. URL: http://dx.doi.org/10.1007/s00445-007-0184-8. doi:10.1007/s00445-007-0184-8.

M. Polacci, D. R. Baker, L. Mancini, S. Favretto, R. J. Hill, Vesiculation in magmas from stromboli and implications for normal strombolian activity and paroxysmal explosions in basaltic systems, Journal of Geophysical Research: Solid Earth

114 (2009). URL: http://dx.doi.org/10.1029/2008JB005672. doi:10.1029/2008jb005672.

M. Polacci, D. R. Baker, A. La Rue, L. Mancini, P. Allard, Degassing behaviour of vesiculated basaltic magmas: an example from ambrym volcano, vanuatu arc, Journal of Volcanology and Geothermal Research 233–234 (2012) 55–64. URL: http://dx.doi.org/10.1016/j.jvolgeores.2012.04.019. doi:10.1016/j.jvolgeores.2012.04.019.

A. E. Lange, R. L. Nielsen, F. J. Tepley, A. J. R. Kent, The petrogenesis of plagioclase-phyric basalts at mid-ocean ridges, Geochemistry, Geophysics, Geosystems 14 (2013) 3282–3296. URL: http://dx.doi.org/10.1002/ggge.20207. doi:10.1002/ggge.20207.

M. L. Coombs, J. C. Eichelberger, M. J. Rutherford, Experimental and textural constraints on mafic enclave formation in volcanic rocks, Journal of Volcanology and Geothermal Research 119 (2003) 125–144. URL: http://dx.doi.org/10.1016/S0377-0273(02)00309-8. doi:10.1016/s0377-0273(02)00309-8.

C. R. Bacon, Magmatic inclusions in silicic and intermediate volcanic rocks, Journal of Geophysical Research: Solid Earth 91 (1986) 6091–6112. URL: http://dx.doi.org/10.1029/JB091iB06p06091. doi:10.1029/jb091ib06p06091.

P. A. Candela, Physics of aqueous phase evolution in plutonic environments, American Mineralogist 76 (1991) 1081–1091.

N. Roduit, JMicroVision: Image analysis toolbox for measuring and quantifying components of high-definition images, 2008. https://jmicrovision.github.io.

O. Higgins, M. J. Stock, A New Calibration of the OPAM Thermobarometer for Anhydrous and Hydrous Mafic Systems, Journal of Petrology 65 (2024). URL: http://dx.doi.org/10.1093/petrology/egae043. doi:10.1093/petrology/egae043.

R. Subbaraman, M. Hartley, D. A. Neave, Thin section scans of gabbro nodules, scoria, plagioclase-phyric basalt, hyaloclastite from Gígöldur, central Iceland, Figshare. DOI: https://doi.org/10.48420/28435859.v1, 2025a. URL: https://figshare.manchester.ac.uk/articles/figure/Thin_section_scans_of_gabbro_nodules_scoria_plagioclase-phyric_basalt_hyaloclastite_from_G_g_ldur_central_Iceland/28435859.

R. Subbaraman, M. Hartley, M. Polacci, B. Bonechi, L. Pappalardo, G. Buono, D. A. Neave, X-ray computed micro-tomography (XCT) 3D reconstructions of Icelandic gabbro nodules, Figshare. DOI: https://doi.org/10.48420/28435859.v1, 2025b. URL: https://figshare.manchester.ac.uk/articles/figure/X-ray_computed_micro-tomography_XCT_3D_reconstructions_of_Icelandic_gabbro_nodules/28431773.

C. Klug, K. V. Cashman, Permeability development in vesiculating magmas: implications for fragmentation, Bulletin of Volcanology 58 (1996) 87–100. URL: http://dx.doi.org/10.1007/s004450050128. doi:10.1007/s004450050128.

R. S. J. Sparks, S. Brazier, New evidence for degassing processes during explosive eruptions, Nature 295 (1982) 218–220. URL: http://dx.doi.org/10.1038/295218a0. doi:10.1038/295218a0.

E. Bali, M. E. Hartley, S. A. Halldórsson, G. H. Gudfinnsson, S. Jakobsson, Melt inclusion constraints on volatile systematics and degassing history of the 2014–2015 holuhraun eruption, Iceland, Contributions to Mineralogy and Petrology 173 (2018). URL: http://dx.doi.org/10.1007/s00410-017-1434-1. doi:10.1007/s00410-017-1434-1.

D. A. Neave, J. Maclennan, M. Edmonds, T. Thordarson, Melt mixing causes negative correlation of trace element enrichment and CO2 content prior to an Icelandic eruption, Earth and Planetary Science Letters 400 (2014) 272–283. URL: http://dx.doi.org/10.1016/j.epsl.2014.05.050. doi:10.1016/j.epsl.2014.05.050.

M. Le Voyer, E. H. Hauri, E. Cottrell, K. A. Kelley, V. J. M. Salters, C. H. Langmuir, D. R. Hilton, P. H. Barry, E. Füri, Carbon fluxes and primary magma co2contents along the global mid-ocean ridge system, Geochemistry, Geophysics, Geosystems 20 (2019) 1387–1424. URL: http://dx.doi.org/10.1029/2018GC007630. doi:10.1029/2018gc007630.

S. Matthews, O. Shorttle, J. Maclennan, J. F. Rudge, The global melt inclusion c/ba array: Mantle variability, melting process, or degassing?, Geochimica et Cosmochimica Acta 293 (2021) 525–543. URL: http://dx.doi.org/10.1016/j.gca.2020.09.030. doi:10.1016/j.gca.2020.09.030.

E. H. Hauri, J. Maclennan, D. McKenzie, K. Gronvold, N. Oskarsson, N. Shimizu,

CO2 content beneath northern Iceland and the variability of mantle carbon, Geology 46 (2017) 55–58. URL: http://dx.doi.org/10.1130/G39413.1. doi:10.1130/g39413.1.

V. Martin, D. Pyle, M. Holness, The role of crystal frameworks in the preservation of enclaves during magma mixing, Earth and Planetary Science Letters 248 (2006) 787–799. URL: http://dx.doi.org/10.1016/j.epsl.2006.06.030. doi:10.1016/j.epsl.2006.06.030.

L. Bai, D. R. Baker, M. Rivers, Experimental study of bubble growth in stromboli basalt melts at 1 atm, Earth and Planetary Science Letters 267 (2008) 533–547. URL: http://dx.doi.org/10.1016/j.epsl.2007.11.063. doi:10.1016/j.epsl.2007.11.063.

G. Iacono-Marziano, Y. Morizet, E. Le Trong, F. Gaillard, New experimental data and semi-empirical parameterization of h2o–co2 solubility in mafic melts, Geochimica et Cosmochimica Acta 97 (2012) 1–23. URL: http://dx.doi.org/10.1016/j.gca.2012.08.035. doi:10.1016/j.gca.2012.08.035.

K. Iacovino, S. Matthews, P. E. Wieser, G. M. Moore, F. Bégué, Vesical part i: An open-source thermodynamic model engine for mixed volatile (h2o-co2) solubility in silicate melts, Earth and Space Science 8 (2021). URL: http://dx.doi.org/10.1029/2020EA001584. doi:10.1029/2020ea001584.

W. Degruyter, A. Parmigiani, C. Huber, O. Bachmann, How do volatiles escape their shallow magmatic hearth?, Philosophical Transactions of the Royal Society A: Mathematical, Physical and Engineering Sciences 377

(2019) 20180017. URL: http://dx.doi.org/10.1098/rsta.2018.0017. doi:10.1098/rsta.2018.0017.

J. Jenkins, J. Maclennan, R. G. Green, S. Cottaar, A. F. Deuss, R. S. White, Crustal formation on a spreading ridge above a mantle plume: Receiver function imaging of the icelandic crust, Journal of Geophysical Research: Solid Earth 123 (2018) 5190–5208. URL: http://dx.doi.org/10.1029/2017JB015121. doi:10.1029/2017jb015121.

K. D. Putirka, Thermometers and barometers for volcanic systems, Reviews in Mineralogy and Geochemistry 69 (2008) 61–120. URL: http://dx.doi.org/10.2138/rmg.2008.69.3. doi:10.2138/rmg.2008.69.3.

K. Iacovino, C. B. Till, Densityx: A program for calculating the densities of magmatic liquids up to 1,627 °c and 30 kbar, Volcanica 2 (2019) 1–10. URL: http://dx.doi.org/10.30909/vol.02.01.0110. doi:10.30909/vol.02.01.0110.

R. A. Lange, A revised model for the density and thermal expansivity of k 2 o-na 2 o-cao-mgo-al 2 o 3 -sio 2 liquids from 700 to 1900 k: extension to crustal magmatic temperatures, Contributions to Mineralogy and Petrology 130 (1997) 1–11. URL: http://dx.doi.org/10.1007/s004100050345. doi:10.1007/s004100050345.

R. A. Lange, I. S. Carmichael, Densities of na2o-k2o-cao-mgo-feo-fe2o3-al2o3-tio2-sio2 liquids: New measurements and derived partial molar properties, Geochimica et Cosmochimica Acta 51 (1987) 2931–2946.

URL: http://dx.doi.org/10.1016/0016-7037(87)90368-1. doi:10.1016/0016-7037(87)90368-1.

X. Guo, R. A. Lange, Y. Ai, Density and sound speed measurements on model basalt (an–di–hd) liquids at one bar: New constraints on the partial molar volume and compressibility of the feo component, Earth and Planetary Science Letters 388 (2014) 283–292. URL: http://dx.doi.org/10.1016/j.epsl.2013.12.005. doi:10.1016/j.epsl.2013.12.005.

F. A. Ochs III, R. A. Lange, The density of hydrous magmatic liquids, Science 283 (1999) 1314–1317. URL: http://dx.doi.org/10.1126/science.283.5406.1314. doi:10.1126/science.283.5406.1314.

V. C. Kress, I. S. E. Carmichael, The compressibility of silicate liquids containing fe2o3 and the effect of composition, temperature, oxygen fugacity and pressure on their redox states, Contributions to Mineralogy and Petrology 108 (1991) 82–92. URL: http://dx.doi.org/10.1007/bf00307328. doi:10.1007/bf00307328.

R. G. Berman, Internally-consistent thermodynamic data for minerals in the system Na2O-K2O-CaO-MgO-FeO-Fe2O3-Al2O3-SiO2-TiO2-H2O-CO2., Journal of Petrology 29 (1988) 445–522. URL: http://dx.doi.org/10.1093/petrology/29.2.445. doi:10.1093/petrology/29.2.445.

J. R. Smyth, T. C. McCormick, Crystallographic Data for Minerals, AGU Reference Shelf, American Geophysical Union, 1995, pp. 1–17.

S. P. Jakobsson, K. Jónasson, I. A. Sigurðsson, The three igneous rock series of iceland, Jökull 58 (2008) 117–138.

H. Jóhannesson, K. Sæmundsson, Geological map of iceland: Tectonics, 2009. 1:600,000, revised edition.

Google Earth Pro, Satellite imagery of gígöldur, iceland, https://earth.google.com/, 2025. Data provided by Maxar Technologies, CNES/Airbus.

M. A. Sigurgeirsson, Árni Hjartarson, I. Kaldal, K. S. mundsson, S. ur Garð ar Kristinsson, S. Víkingsson, Geological map of the northern volcanic zone, iceland. southern part, 2015.